The Astrophysical Journal, 646:1303–1318, 2006 August 1

PHOTOSPHERIC MAGNETIC FIELD PROPERTIES OF FLARING VERSUS FLARE-QUIET ACTIVE REGIONS. III. MAGNETIC CHARGE TOPOLOGY MODELS

G. Barnes and K. D. Leka
Colorado Research Associates Division, NorthWest Research Associates, Inc., 3380 Mitchell Lane, Boulder, CO 80301;
graham@cora.nwra.com, leka@cora.nwra.com
Received 2005 June 3; accepted 2006 April 7

ABSTRACT

A magnetic charge topology (MCT) model is applied to time series of photospheric vector magnetic field data for seven active regions divided into epochs classified as flare-quiet and flare-productive. In an approach that parallels an earlier study by the authors using quantities describing the photospheric properties of the vector magnetic field, we define quantities derived from the MCT analysis that quantify the complexity and topology of the active region coronal fields. With the goal of distinguishing between flare-quiet and flare-imminent magnetic topology, the time series are initially displayed for three active regions for visual inspection with few clear distinguishing characteristics resulting. However, an analysis of all 24 epochs using the discriminant analysis statistical approach indicates that coronal field topology, derived from the observed photospheric vertical field, may indeed hold relevant information for distinguishing these populations, although the small sample size precludes a definite conclusion. The variables derived from the characterization of coronal topology routinely result in higher probabilities of being able to distinguish between the two populations than the analogous variables derived for the photospheric field.

Subject headings: Sun: activity — Sun: corona — Sun: flares — Sun: magnetic fields — Sun: photosphere

1. INTRODUCTION

Although the storage and release of the energy that powers solar flares is generally believed to be in the coronal magnetic field, most studies have focused directly on the photospheric properties of the host region (e.g., recently Falconer et al. 2003; Abramenko et al. 2003; Leka & Barnes 2003a [hereafter Paper I], 2003b [hereafter Paper II] and references therein). This is a natural first step, since it is the photospheric magnetic field that is typically measured, and many of the photospheric properties considered have implications for the coronal magnetic field. For example, the magnetic shear has implications for the amount of magnetic free energy available to power a flare. Here we use photospheric vector magnetic field measurements to infer the coronal magnetic topology, with particular emphasis on properties of the coronal field necessary for magnetic reconnection.

A number of approaches to examining the coronal topology have been developed, including many variations focusing on quasi separatrix layers (Priest & Démoulin 1995), but here we focus on the approach known as magnetic charge topology (MCT; Baum & Bratenahl 1980; Gorbachev & Somov 1988; Priest & Forbes 1989; Lau 1993; Démoulin et al. 1994; Parnell et al. 1994). MCT models provide a particularly simple context for magnetic reconnection and have had some success in predicting the locations for solar flares (Mandrini et al. 1991; Démoulin et al. 1993; Longcope & Silva 1998).

In this class of model, each concentration of photospheric flux is represented by a single point source, and the magnetic field above the photosphere is taken to be that due only to the collection of point sources. Implementing the model begins by partitioning the vertical component of the photospheric field to identify flux concentrations. In the specific model we employ (Barnes et al. 2005, hereafter BLL), sources are placed in the plane of the photosphere, with the flux of each source equal to the flux contained within its corresponding partition. This approach has the advantage of being able to quantify real changes in the connectivity of the coronal field. Other implementations of MCT, in which subphotospheric sources are employed, may reproduce individual field lines more accurately, but are less suitable for tracking those changes in the magnetic flux critical to reconnection.

By reducing the extrapolated coronal field to that due to a collection of coplanar point sources, characterizing the topology is greatly simplified. Field lines can only have end points on photospheric sources, except for certain crucial exceptions discussed below. Bundles of field lines connecting one source with another source of opposite polarity are known as domains, and each domain is enclosed by separatrix surfaces. Separatrices are also associated with locations where the field vanishes, known as null points. In the vicinity of a null point $\boldsymbol{x}_a$, the field can be expressed as

$$\boldsymbol{B}(\boldsymbol{x}_a + \delta\boldsymbol{x}) \approx \boldsymbol{M}^a \cdot \delta\boldsymbol{x}, \tag{1}$$

where $\boldsymbol{M}^a_{ij} = \partial B_i/\partial x_j$ is the Jacobian matrix evaluated at $\boldsymbol{x}_a$. The two eigenvectors of the Jacobian with the same sign define a plane known as the fan surface, while the eigenvector of opposite sign defines the spine field lines. A-type (B type) nulls have a positive (negative) spine eigenvector, while a photospheric null is defined as prone if the spine lies in the plane of the photosphere and upright otherwise. Field lines in the fan surface of a null point lie on a separatrix surface. The intersection of two separatrices is known as a separator, which is a field line that originates and terminates on two null points. In this simplified model, reconnection takes the form of the exchange of footpoints for a pair of field lines, thus involving four domains connecting two pairs of sources. During reconnection, flux moves from one pair of domains to the other pair across a separator field line, where the four domains come together, preserving the magnitudes of all the sources. Thus, separator field lines are particularly interesting in MCT models as the location of any reconnection.

In BLL, we demonstrated how an MCT model can be applied to observed time series of photospheric vector magnetic field data, accounting for variations in atmospheric seeing, as well as

TABLE 1
Active Regions and Epochs Data Summary

NOAA AR Number	Date	Coordinates	Magnitude Class	Start Time	End Time	Event
8210	1998 May 1	S18 W05	$\beta\gamma$	17:07	18:07	
				18:15	19:14	
				19:31	20:08	C2.8
				20:11	21:35	C2.6
				21:55	22:35	M1.2
				22:38	23:25	
8636	1999 Jul 23	N20 E04	$\beta\gamma\delta$	16:47	18:31	M1.1
				18:35	18:50	
				19:14	19:30	
				20:09	20:28	
				21:04	22:11	
8771	1999 Nov 25	S15 W48	$\beta\gamma$	18:13	18:38	C1.6
				18:42	18:58	M2.0
				19:02	19:34	
8891	2000 Mar 1	S15 E11	$\beta\gamma$	18:13	19:07	
				19:43	20:38	
				20:49	21:24	
9026	2000 Jun 5	N22 E20	$\beta\gamma\delta$	17:06	18:22	C3.8
				18:25	18:57	
9165	2000 Sep 15	N13 E03	$\beta\gamma$	19:44	20:51	C7.4
				20:55	21:18	
10030	2002 Jul 15	N18 E03	$\beta\gamma\delta$	18:53	19:58	X3.0
				20:02	21:02	M1.8
				22:04	22:24	

uncorrelated noise. In order to minimize changes in the partitioning due to noise, a reference magnetogram was constructed for the time series, and the partitioning at each time within the series was constructed so as to minimize the difference between it and the reference. Without the use of a reference magnetogram, systematic changes tend to occur in the partitioning as the seeing changes. In particular, the number of sources decreases as the seeing degrades, effectively because the blurring of the images reduces the distinction between individual flux concentrations. By comparing all magnetograms in a time series to a single reference, the systematic effects of the variations in seeing are mitigated, while the real evolution of the solar magnetic field is hopefully still captured.

Aside from determining the partitioning for each time step based on the reference, the time steps are considered individually, with no regard for how the field would evolve from one to the next. For this approach to be accurate, reconnection would have to proceed faster than the domain fluxes change due to evolution of the sources. However, based on the microscopic conductivity of the coronal plasma, this is unlikely to be the case, so each domain flux should remain nearly constant. Instead of reconnection, currents begin to flow in the corona. Longcope (1996) showed that the lowest energy configuration in the context of MCT models contains currents only along separator field lines; he dubbed this the minimum current corona (MCC) model.

In essence, current flowing in a separator loop induces just enough magnetic flux, in accordance with Faraday's law, to cancel the change in flux due to the motion of the sources. The initial effect of the motion of the sources is to cause currents to flow along the separators. However, if the current along any separator builds up to a sufficiently large value, it is hypothesized that an instability will occur, such as the ion-acoustic instability or the tearing mode (Longcope & Silva 1998). The instability can lead to large anomalous resistivities that allow reconnection to proceed extremely rapidly, resulting in a flare. This technique has been applied to one observational example (Longcope & Silva 1998), where it had some success in predicting the locations of Hα and soft and hard X-ray brightenings. It has also been compared to the results of a line-tied ideal magnetohydrodynamic (MHD) simulation of a relatively simple configuration (Longcope & Magara 2004), and good agreement was found between the resulting currents.

As a first step, we use the results of MCT to quantify magnetic complexity in terms of the richness of coronal interconnections, and where possible we interpret this in the context of the MCC model. Having mapped the source locations and strengths, the locations of magnetic null points, the magnetic connectivity, and the magnetic separator field lines, the question now posed is whether this topological information can, in fact, be used to characterize an active region's magnetic state as flare-imminent or flare-quiet. According to MCT models, a field with more connections per source will have more separators and will therefore have more options for reconnection. But is it simply a matter of the number of separators that distinguishes a flare-productive active region? We present, in the same manner as Leka & Barnes (Paper I), parameterizations of the information obtained by MCT analysis, such that a detailed examination of the spatial distributions of the active region's magnetic connectivity and nulls, locations of separators, etc., is not necessary. After presenting the parameterizations, we apply discriminant analysis to time series data from seven active regions, in an manner analogous to Leka & Barnes (Paper II). Even though each of the time series is divided into several epochs that are analyzed independently, our sample size is still only 24. This is too small to draw definite conclusions about what parameters may best relate to flare activity, but by using the same sample as in Paper II, we believe we can make meaningful comparisons between parameters describing the photosphere and those describing the coronal topology.

2. DATA AND ANALYSIS SUMMARY

As in Paper I, we present an initial description and examples of the parameterizations for three of our target active regions (NOAA Active Regions 8636, 8891, and 10030; see Table 1), each comparable in overall size, magnetic classification, and flare production. For this initial demonstration, the focus is on three flares (two M class and one X class) that occurred during observations of two of the active regions (AR 8636 and 10030) and (most importantly) a flare-quiet period of observation of the third active region (AR 8891). For the discriminant analysis portion, paralleling the approach detailed in Paper II, we apply the parameterizations of the MCT model to all seven active region time series that are divided into the 24 epochs summarized in Table 1. Each epoch in the time series is determined to end with either the occurrence of a flare, a gap of longer than 20 minutes in the data, or a shorter gap after more than an hour of continuous data.

The observational data used for this study are time series of photospheric vector magnetic field maps from the University of Hawaii Mees Solar Observatory Imaging Vector Magnetograph (IVM). After initial data reduction, the ambiguity in the image plane transverse field is solved essentially following the University of Hawaii iterative procedure (Canfield et al. 1993), with additional constraints for temporal consistency. The resulting heliographic plane maps of the vertical component of the field, B_z, form the input to the MCT model analysis. Additional details concerning the data and its processing for this project are described in Mickey et al. (1996), LaBonte et al. (1999), and Paper I.

For each epoch, we use the approach of BLL to determine the basic building blocks of the MCT model, from which a variety of parameters are constructed that quantify the coronal topology. First, a reference magnetogram is constructed from the time-averaged value of the vertical field at each (co-aligned) pixel, discarding those areas in which the smoothed field is consistent with zero. The reference magnetogram is partitioned by assigning to each pixel a region label based on a gradient-based tesselation scheme, so that the pixel ends up with the same label as the local maximum in $|B_z|$ from which it is downhill. This approach can lead to an excessively large number of very small partitions in plage, so the results are simplified by merging partitions containing flux less than 1×10^4 G Mm^2 with a neighboring partition of the same polarity and by merging partitions that are separated by a saddle point at which the vertical field strength is less than 100 G different from either of the local maxima. This approach simplifies the plage regions, while maintaining the structure in strong field regions. Since the domain fluxes associated with any small partition must also be small, we believe that this approach does not greatly affect the estimation of the connectivity of the magnetic field, which is our primary concern.

Each magnetogram in the epoch is partitioned by minimizing the difference with the reference partitioning. A source is assigned to each partition, with a flux, Φ_i, equal to the flux contained in the partition at a location $\boldsymbol{x}_i$ given by the flux-weighted average position of the partition.

Having determined the properties of the sources, we wish to characterize the coronal topology. To do this, field lines are initiated in random directions from each source and traced to their termination on a source of the opposite polarity. A Bayesian estimate is used for the connectivity matrix, ψ_{ij}, whose elements give the amount of flux connecting source i to source j, based on the number of field lines found to connect the pair of sources. By choosing the number of field lines initiated at each source to be proportional to the source flux, a consistent flux threshold, ψ_c, is established, above which 95% of the connections are expected to be found. For the results presented here, the connectivity is calculated with $\psi_c = 1.5 \times 10^{17}$ Mx, which requires of order 10^6 field lines to be traced for each magnetogram. Our more precise calculations in BLL for AR 8210 indicate that this threshold is likely to find the majority of the connections.

The null points are located using a Newton-Raphson root-finding algorithm, with initial locations based on considering pairs and triplets of sources in isolation (see BLL for details). Knowing the location of a null point, the eigenvectors and eigenvalues of the Jacobian matrix are determined at that point to characterize the type of the null and to determine its spines and fan surface. Tracing the spine field lines associates a pair of sources with the null.

Separator field lines are the intersections of two fan surfaces, and they thus connect a pair of nulls. The first step in finding the separators is to determine which nulls are linked. This is done by initiating field lines in the fan surface of a null; if neighboring field lines in the fan surface terminate on different sources, they must bracket at least one separator. A pair of nulls is linked if the spine sources of one null match sources in the fan surface of the other null (see BLL, Fig. 5). Our null-linking algorithm refines the location of a separator in the fan surface to a typical range in angle of 9.4×10^{-11}. While this may seem like extremely high precision, even greater precision is necessary to locate all the separators. For comparison, in BLL, we refined the separator locations to lie in a range in angle of 1.9×10^{-12} and located about 10% more separators in AR 8210. However, the missing separators are generally associated with at least one domain that has very little flux.

Once a separator is located, it is identified by the pair of nulls that it links and by the angle in the fan surface that it makes at each null. Further properties of the separators can be determined, including the length, l_i, and maximum height, z_i, as well as the flux enclosed by the separator, Ψ_i, which is a roughly equivalent characterization of the topology of the corona to that given by the connectivity.

Examples of the MCT properties from the three active regions are shown in Figure 1. The left column shows how each region is partitioned based on the flux concentrations and the location of the source associated with each partition. Our partitioning algorithm is able to retain small intrusions of opposite polarity flux, such as δ-spots, while simplifying regions of plage to a tractable number of sources. An example of such an intrusion is visible in the figure of AR 8636 at $(x, y) \approx (-80, 240)$. The right column shows the null points (*triangles*) and separator field lines (*green*). Evidently, the topology of all three regions is quite complicated, but is there any quantitative way to distinguish the complexity needed to produce a flare?

3. FLARE-PREDICTING PARAMETERS

Our goal is to quantitatively characterize the properties an active region must possess in order to undergo a flare event. We include parameters that represent three broad categories with some overlap. The first category simply measures the overall complexity of a region. If the reconnection that powers a flare is a means of simplifying the topology of the coronal field, then presumably the field must start with a certain amount of complexity. The second category looks for a trigger for a flare. For example, the emergence of new flux into an existing active region is thought to be a mechanism for triggering a flare. Finally, if flares are indeed associated with reconnection along a separator, then separators must be present in an active region in an appropriate location associated with sufficient magnetic energy, etc. We therefore consider the number and morphology of locations where a flare could occur.

As with quantities describing the photospheric vector magnetic field itself, such as the distribution of magnetic flux, the vertical current densities, etc., that were the focus of Papers I and II, the goal is to parameterize the quantities that have a spatial

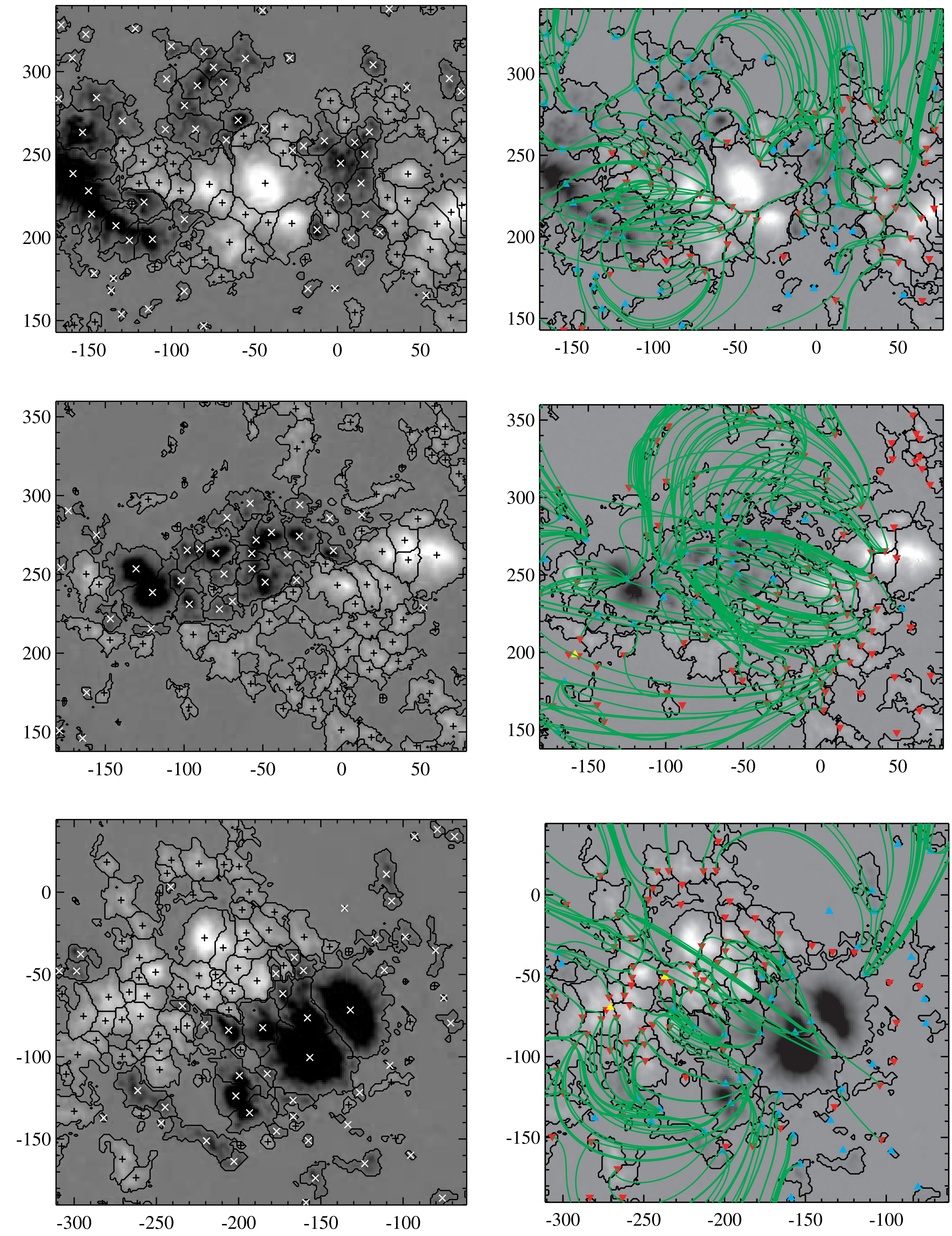

FIG. 1.—Images of the vertical field (*gray scale*), along with various features of the MCT model for NOAA AR 10030 with 113 sources (*top*), AR 8636 with 116 sources (*middle*) , and AR 8891 with 126 sources (*bottom*). The left panels show how the region is partitioned, and each of the sources (plus signs indicate positive, and crosses indicate negative) for a sample time step. The right panels show null points as triangles, color coded by type (red for A type, blue for B type, and yellow for upright), along with separator field lines (*green*). Axes are scaled in megameters in the image plane, even though all calculations are performed in heliographic coordinates.

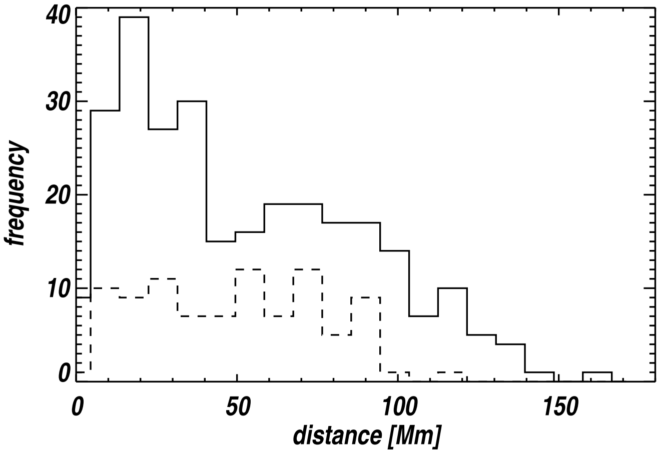

FIG. 2.—Distribution of distance between connected sources for AR 8891. The solid line shows all connected sources, while the dashed line shows only those connected with a flux greater than 5×10^{19} Mx. The distribution for all connected sources has a distinct peak at small distances with a long tail to long distances, compared with a relatively flat distribution for only the large-flux connections. This is reflected in, for example, the much larger unweighted skew of the distribution compared to the weighted skew.

component in order to eventually allow for completely objective evaluation. To achieve this, we follow Paper I and employ the first four moments (mean, standard deviation, skew, and kurtosis) to describe the distributions of many of our parameters; when applicable, relevant summations are also used. We frequently are interested only in those sources that are connected, and so we weight the moments of some of our parameters by the domain flux in the following fashion:

$$\text{weighted mean } \overline{(x, w)} = \frac{\sum_i w_i x_i}{\sum_i w_i}, \tag{2}$$

$$\text{weighted standard deviation } \sigma(x, w) = \left[\frac{\sum_i w_i (x_i - \overline{x})^2}{\sum_i w_i}\right]^{1/2}, \tag{3}$$

$$\text{weighted skew } \varsigma(x, w) = \frac{\sum_i w_i (x_i - \overline{x})^3 / \sigma^3}{\sum_i w_i}, \tag{4}$$

$$\text{weighted kurtosis } \kappa(x, w) = \frac{\sum_i w_i (x_i - \overline{x})^4 / \sigma^4}{\sum_i w_i} - 3, \tag{5}$$

where w_i is the weighting factor, which typically is taken to be the domain flux. The mean and standard deviation are familiar quantities describing a typical value for the distribution and the spread about that value. The higher order moments are constructed to vanish for a Gaussian distribution, and nonzero values describe how a distribution deviates from Gaussian. In particular, the third moment, skewness, describes the asymmetry of a distribution and is a signed quantity sensitive to the presence of a one-sided tail in the distribution. The kurtosis reflects the presence (or absence) of two-sided tails in the distribution. Physically, the skew and kurtosis may be thought of as reflecting properties of localized parts of the region that have values far from the mean.

In Figure 2, we show a sample distribution of the distance between connected sources for NOAA AR 8891, along with the weighted and unweighted moments of the distribution in Table 2. The solid line shows the distribution of distance between all connected sources, while the dashed line shows the distance for those sources connected by a flux of at least 5×10^{19} Mx. The distribution for all connected sources has a distinct peak at a distance of about 20 Mm, with a tail extending out past 150 Mm, which produces the relatively large unweighted skew of 0.58. In comparison, only the large-flux connections exhibit a relatively flat distribution between about 10 and 100 Mm. This is manifest in the much smaller weighted skew of 0.12. Thus, we frequently employ the moments weighted by the flux in a connection, as this will emphasize the properties of the large-flux connections.

TABLE 2
Weighted and Unweighted Moments

	Mean	Standard Deviation	Skew	Kurtosis
Weighted	59.86	28.08	0.1177	−0.7463
Unweighted	59.92	38.01	0.5781	−0.6434

To determine the uncertainty in the moments of the various distributions, we start with the uncertainties in the sources, nulls, separators, and flux in connections. The main source of uncertainty for most of the parameters is the partitioning of the magnetogram. To quantify how this uncertainty enters into the parameters, we look at the variations in the time series, following the approach described in detail in BLL, although in some cases, as discussed above, the precision is less than in BLL for computational reasons. We then use a formal propagation of errors to determine the uncertainty in each of the moments of the various distributions. The results are used for plotting the error bars in the epochs presented. The formal propagation of errors typically results in a value that is comparable to the least-squares deviation about a linear fit to each epoch.

As with the parameterization undertaken in Paper I of quantities describing the photospheric vector field, the goal is to adequately describe the situation without relying on visual or other subjective analysis. That is, we turn a complicated image into one or a few numbers that can be quantitatively compared between active regions and epochs. Below, we describe the parameters derived from the MCT model. Others certainly could be derived and hopefully will be as this model and technique are explored further. For the moment, we present the following parameterizations, which are summarized in Table 3. Note that the moment analysis is performed only for a parameter x if listed in the table as $\mathcal{M}(x)$; in some cases, we consider the total of a parameter in addition to its moments, in which case the total is listed as a separate variable in the table.

3.1. *Number of Sources and Their Flux Distribution*

Perhaps the simplest measure of the complexity of the coronal field is the number of poles, or sources S, used to generate it (Table 3). To the extent that each partition may be thought of as representing a bundle of magnetic flux passing through the photosphere, the number of sources tracks how many flux tubes compose the active region. Due to the reference magnetogram method employed to mitigate changes due to seeing and random noise fluctuations, the number of sources is set to be essentially constant during an epoch (BLL). However, each source is also described by a location and a charge, effectively, the magnetic flux associated with each partition. Thus, the case of emerging flux will generally manifest not as additional sources during an epoch, but rather as increasing flux for a source that is allowed

TABLE 3
MCT Parameters Used in the Discriminant Analysis

Description	Formula	Variable
Number of sources		S
Distribution of source flux:		
Moments of unsigned source flux		$\mathcal{M}(\lvert\Phi_i\rvert)$
Magnetostatic energy	$E_B = \sum_{i<j} q_i q_j / \lvert \boldsymbol{x}_i - \boldsymbol{x}_j \rvert$	E_B
Distribution of connectivity:		
Moments of number of connections per pole		$\mathcal{M}(C_i)$
Total number of connections	$C = \sum C_i$	C
Number of connections to infinity		C_∞
Distribution of domain flux:		
Moments of flux in each connection		$\mathcal{M}(\psi_{ij})$
Distribution of flux-weighted distance:		
Moments of distance between sources weighted by flux	$r_{ij} = \lvert \boldsymbol{x}_i - \boldsymbol{x}_j \rvert$	$\mathcal{M}(r_{ij}, \psi)$
Distribution of flux per distance:		
Moments of flux per distance	$\varphi_{ij} = \psi_{ij} / \lvert \boldsymbol{x}_i - \boldsymbol{x}_j \rvert$	$\mathcal{M}(\varphi_{ij})$
Total flux per distance	$\varphi_{\rm tot} = \sum \varphi_{ij}$	$\varphi_{\rm tot}$
Flux-weighted distribution of tilt angle:		
Moments of tilt angle weighted by flux	$\xi_{ij} = \tan^{-1}[(y_j - y_i)/(x_j - x_i)]$	$\mathcal{M}(\xi_{ij}, \psi)$
Number of nulls:		
Number of prone nulls		N_{p0}
Number of upright nulls		N_{u0}
Number of separators:		
Moments of number of separators from each null found		$\mathcal{M}(X_i)$
Total number of separators found	$X = \sum X_i$	X
Length of separators:		
Moments of length of separators found		$\mathcal{M}(l_i)$
Flux enclosed by separators:		
Moments of unsigned flux enclosed by separators found	$\Psi_i = \oint \boldsymbol{A} \cdot \boldsymbol{dl}$	$\mathcal{M}(\lvert\Psi_i\rvert)$
Total unsigned flux enclosed by separators found	$\lvert\Psi\rvert_{\rm tot} = \sum \lvert\Psi_i\rvert$	$\lvert\Psi\rvert_{\rm tot}$
Maximum height of separators:		
Moments of maximum height above photosphere of separators found		$\mathcal{M}(z_i)$
Distribution of multiple domains:		
Number of pairs of nulls with multiple separators		L
Number of extra domains	$D_m = X + S - 1 - C$	D_m

Notes.—$\mathcal{M}(x)$ denotes taking the first four moments of the distribution of the variable x: the mean, $\bar{x}$, the standard deviation, $\sigma(x)$, the skew, $\varsigma(x)$, and the kurtosis, $\kappa(x)$; $\mathcal{M}(x, \psi)$ denotes taking the moments of the distribution of the variable x weighted by the variable ψ. For each of these variables, we consider the mean value for an epoch, denoted by $\langle\ \rangle$, and the slope of a regression line, denoted by d/dt.

due to its presence in the reference magnetogram; rather than being absent, a source may have zero flux at some times in the series.

The source flux distribution for an active region is parameterized by its first four moments. The time series of these moments are shown in Figure 3, covering a few epochs for each of the three active regions (see also Table 3). To avoid hemispheric biases and focus on the size distribution of the sources, we consider here the unsigned flux assigned to each source, $|\Phi_i|$. For each epoch, a new reference magnetogram is constructed, which occasionally leads to fairly significant changes in a parameter. This can be seen, for example, as a small drop in the mean source flux, $\overline{|\Phi_i|}$ (Fig. 3*a*) just after the M1.1 flare for AR 8636. This contrasts with the overall smaller variability observed during much of the rest of the time series that covers two additional epochs. The differences between one epoch and the next in the reference magnetograms are largely a result of different typical atmospheric seeing conditions between the epochs, which lead to systematic changes in the reference magnetograms. In these moments, the variations from epoch to epoch for one region are small compared to the variations from region to region, indicating that the differences between regions are large compared to the effects of seeing on these parameters.

The moments of the source flux show differences between regions of varying magnitude. For example, the mean source flux $\overline{|\Phi_i|}$ has a relatively small range for the three active regions highlighted, between 3 and 5×10^{20} Mx; this is in contrast with the standard deviation of the source fluxes $\sigma(|\Phi_i|)$, which varies by a factor of 2 between the three highlighted regions. With regards to flaring activity, a generally decreasing tend is seen in $\overline{|\Phi_i|}$ for AR 10030 prior to its events, but in AR 8636 there is no such trend. The overall levels of $\overline{|\Phi_i|}$ are consistent between AR 10030 (flare-producing) and AR 8891 (flare-quiet), indicating that this parameter does not identify a flare-productive region uniquely. The standard deviation of the source flux is larger for AR 8891 overall than the other two active regions, a result seen also for the skew and kurtosis. These trends may be contrary to what one might expect, but for these three regions at least, a difference is seen between flare-producing and flare-quiet active regions. In the temporal evolution of the latter three moments, however, no preevent signature is evident. We detail here the evolution of the parameterization of the distribution of source flux and its moments as an illustration, recalling similar discussions in Paper I. Forthwith, example plots will be more selective.

From the locations and fluxes of the sources, we calculate the magnetostatic energy of our collection of magnetic monopoles,

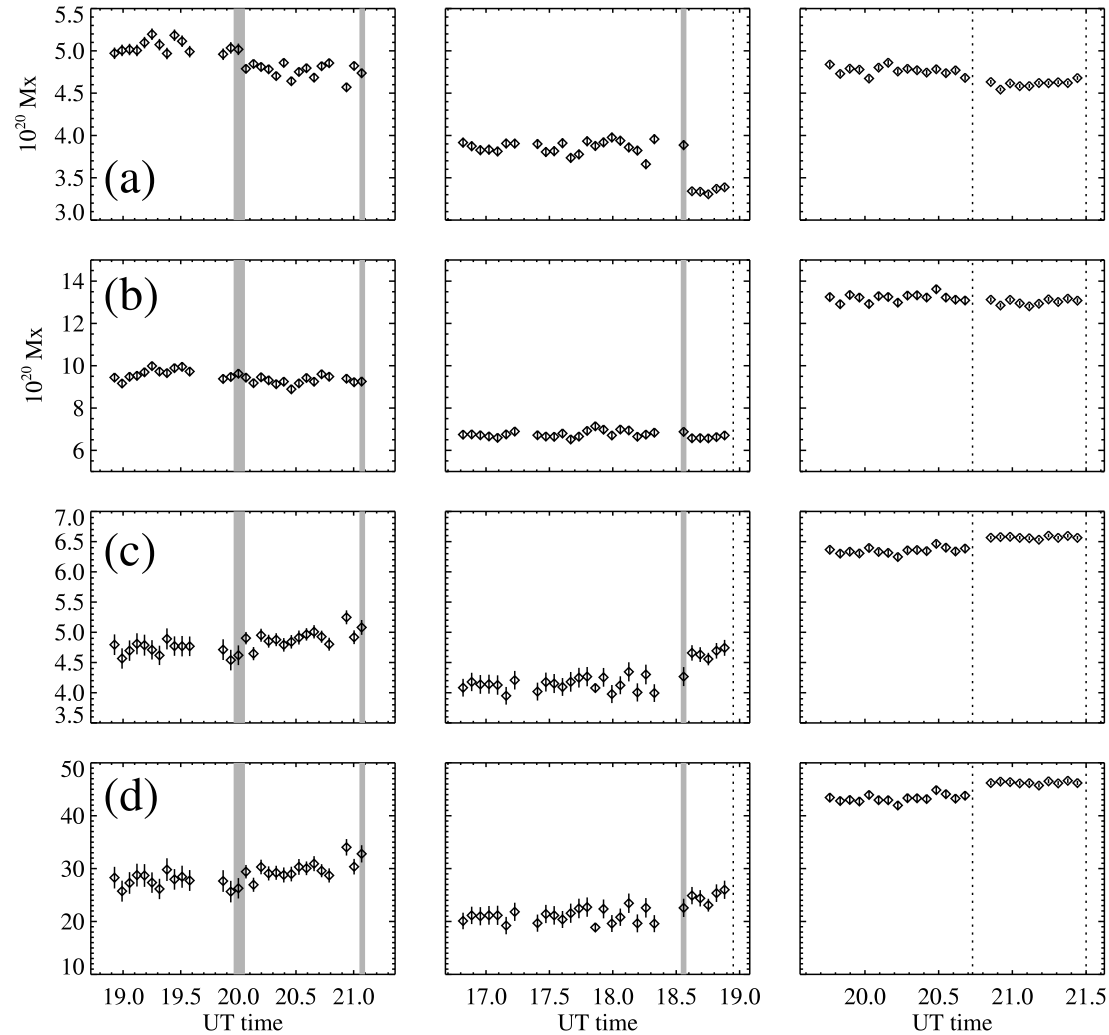

Fig. 3.—Evolution of moments of the distribution of unsigned flux assigned to the magnetic sources for AR 10030 (*left*), AR 8636 (*middle*), and AR 8891 (*right*). The time series have been divided into epochs, with the end of an epoch marked by either a vertical gray line, indicating the start time of a flare as determined by the *GOES* SXR light curve, or by a dotted vertical line, indicating a gap in the data. During the subset of epochs shown, AR 10030 produced X3.0 (*thick gray line*) and M1.8 flares, and AR 8636 produced an M1.1ERU flare, while AR 8891 did not produce any flares. The *x*-axes indicate the UT time, *y*-axes are in the relevant units, and 1 σ error bars are included. For this example, all four moments are shown: (*a*) mean $\overline{|\Phi_i|}$, (*b*) standard deviation $\sigma(|\Phi_i|)$, (*c*) skew $\varsigma(|\Phi_i|)$, and (*d*) kurtosis $\kappa(|\Phi_i|)$. Figs. 4–13 all follow the same format.

in analogy to the electrostatic energy of a collection of point (electric) charges by

$$E_B = \frac{1}{(2\pi)^2} \sum_{i<j} \frac{\Phi_i \Phi_j}{|\boldsymbol{x}_i - \boldsymbol{x}_j|}. \tag{6}$$

If the energy needed for a flare comes from magnetic reconnection, then having a large reservoir of energy available may lead to more or bigger flares. Note that this energy is for a potential field configuration and so does *not* reflect the amount of energy available for release in a flare. As such, the behavior of E_B shown in Figure 4 is somewhat different from our estimate for the excess magnetic energy density given in Paper I. The energy available to power a flare is related to the currents induced along separator field lines in the MCC model. However, a large (potential field) energy implies that a relatively small deviation from the potential field can result in a large amount of free energy; thus we test whether a large potential energy correlates with flare

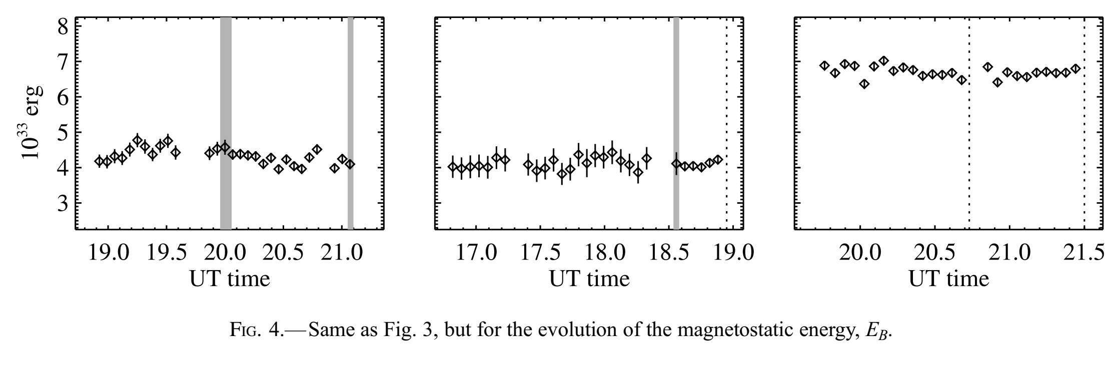

Fig. 4.—Same as Fig. 3, but for the evolution of the magnetostatic energy, E_B.

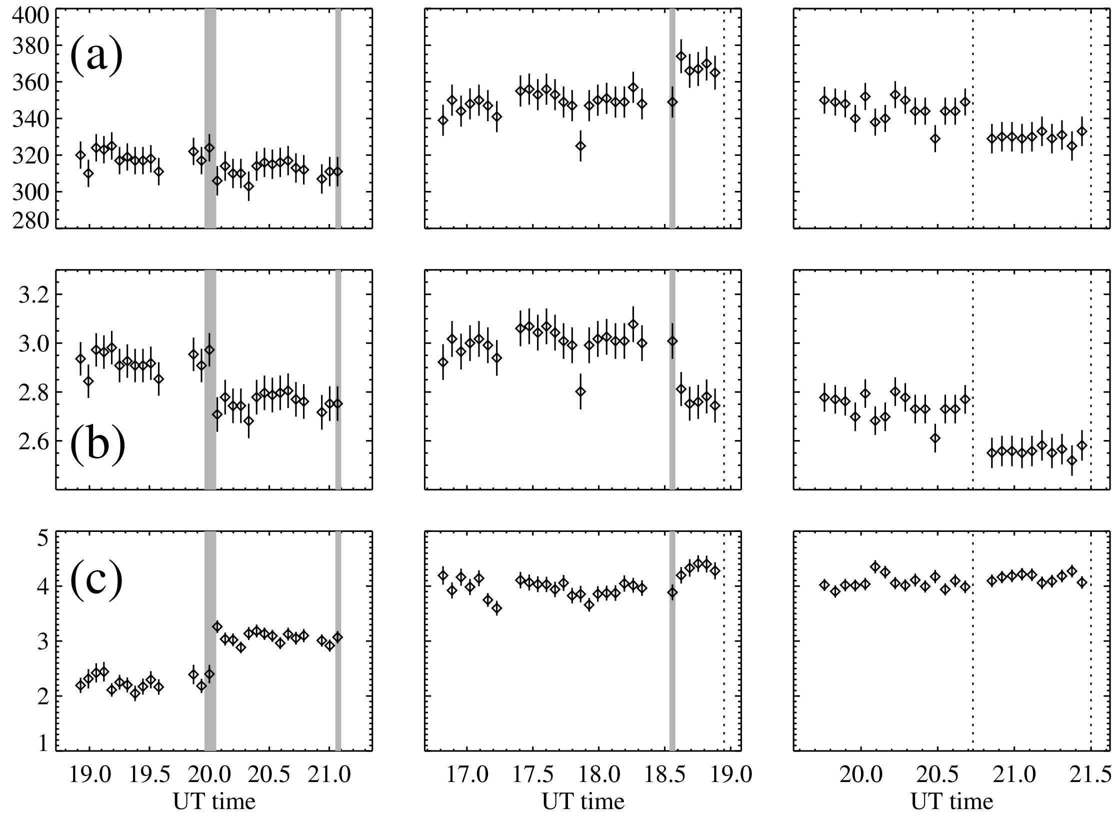

FIG. 5.—Same as Fig. 3, but for (*a*) the total number of connections, C, and two moments of the number of connections per source, (*b*) $\overline{C_i}$, and (*c*) $\varsigma(C_i)$.

activity. Unexpectedly, the threshold of magnetostatic energy appears to be that the flare-quiet region, AR 8891, is larger than the other two. There is also no obvious preevent trend in the time series of this quantity.

3.2. *The Magnetic Connectivity*

One of the direct quantities computed with the MCT approach is the amount of flux in the magnetic connection between each pair of sources. Note that a connection may be composed of more than one domain, so that multiple domains can link the same pair of sources, a point to which we return in § 3.4. The matrix ψ_{ij} consists of the flux connecting source i to source j in a potential field extrapolation. There are two reasons for using this simple extrapolation: (1) modest currents do not greatly affect topological properties, such as the connectivity, and (2) nonpotential alternatives, even such simple ones as linear force-free extrapolations, introduce too many complications for limited gain. Although the potential field extrapolation may not truly represent the complexity, it does well to quantify a lower bound to the true situation. As such, it serves as the basis for numerous parameterizations of the coronal complexity. In particular, reconnection manifests as *changes* in the connectivity, involving the exchange of flux among four connections.

For a region with a complex field topology, we expect that each source will connect to many other sources, and thus we consider the distribution of the number of connections from each source C_i. Higher order moments can test for small, highly complex areas within the region that would not be evident in the mean. For example, a few sources with a large number of connections will result in a large (positive) skew. In Figure 5, we show the total number of connections C for each active region and its evolution. The total number of connections may appear to decrease preevent, but it also appears to decrease slowly in AR 8891's flare-quiescent evolution. All three regions have a large number of connections, with some variation both temporally and between the three; the mean number of connections per source, C_i, is remarkably constant between the three, showing no more variation than between epochs for a single region. In comparison, the skew does show significant variations from region to region, indicating that even though the regions are very similar on average, there must be small areas within some, but not all, regions with enhanced magnetic complexity.

In the MCT model, it is assumed that field lines always begin and end on sources, or null points. However, vector magnetograms invariably exhibit an imbalance between positive and negative magnetic flux within the observed field of view. Thus, an additional source, with flux equal in magnitude but opposite in sign to the net flux in the field of view is placed at infinity to produce zero net flux. Although it is known that active regions generally exhibit magnetic connections to sometimes distant active regions and plage areas, we do not measure these fields and do not have any direct information about them. Thus, at this stage, we consider the number of connections to flux concentrations outside the field of view, C_∞, but we do not consider any of the topological properties of these connections, since they cannot be determined without knowledge of the distribution of flux outside the field of view. Subsequent parameters derived from the location and character of poles and magnetic nulls (see below) only include those that reside close to or within the observed field of view.

We consider the moments of the distribution of flux in each connection ψ_{ij} (an unsigned quantity) as it might relate to the complexity of the active region (Fig. 6). A distribution consisting of many small connections could be indicative of an extremely complex magnetic topology, or it could be representative of many small sources. These scenarios can be distinguished by simultaneously considering the domain flux and the source flux (see § 4).

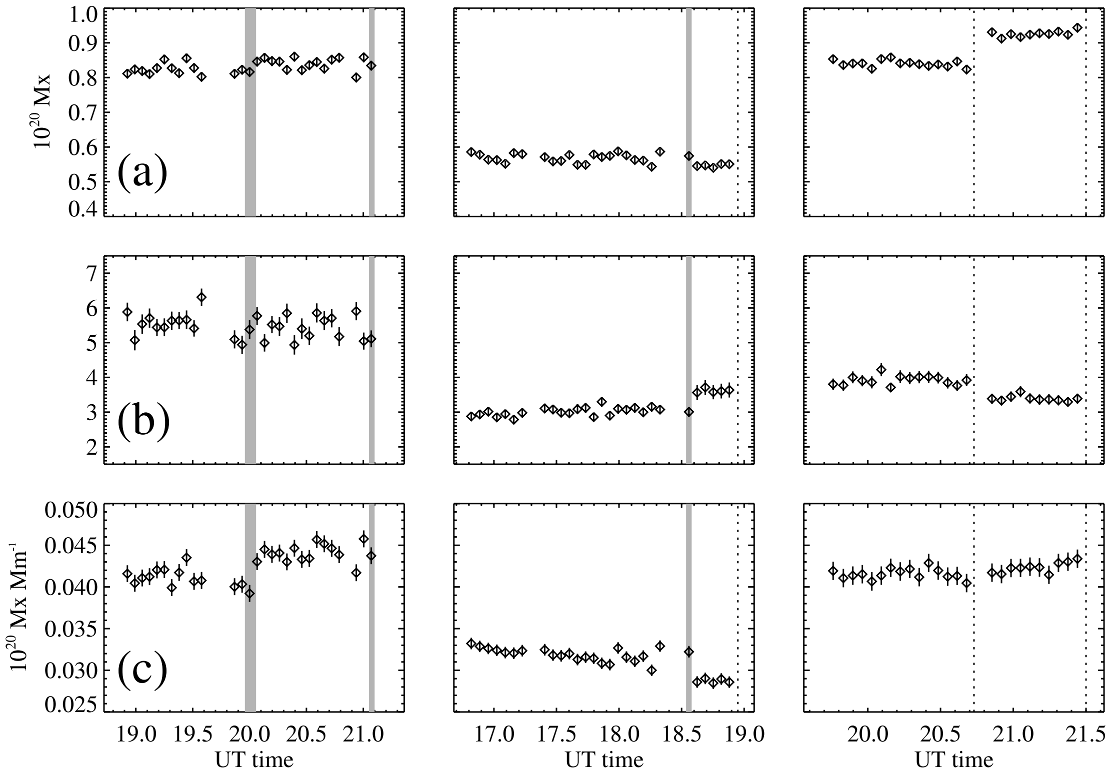

FIG. 6.—Same as Fig. 3, but for moments of the domain flux distribution, (*a*) $\overline{\psi_{ij}}$ and (*b*) $\varsigma(\psi_{ij})$, and (*c*) $\sigma(\varphi_{ij})$, the standard deviation of the domain flux divided by the length of the relevant connection (see text and Table 3).

Anecdotally, the appearance of new flux close to an existing region of opposite polarity, sometimes referred to as a "parasitic polarity," has been invoked as a flare culprit (recently, Aulanier et al. 2000; Liu & Kurokawa 2004; Kundu et al. 2004; Wang 2005; Uddin et al. 2004), and statistically, solar activity is generally associated with emerging magnetic flux (recent studies include Jing et al. 2004). In addition to emerging new flux, converging flows along a neutral line can bring opposite polarity flux together, which is also invoked in certain models for energetic events (e.g., Van Ballegooijen & Martens 1989). As a quantitative test of this, we consider the flux in each connection weighted by the inverse distance,

$$\varphi_{ij} = \frac{\psi_{ij}}{|x_i - x_j|}. \tag{7}$$

In a time series of magnetograms, the mean value of φ_{ij} should increase when new flux emerges, with larger increases for emerging flux close to existing flux. An example is shown in Figure 6; at first glance, there is no unique difference between the flare-quiet and flare-productive regions and epochs. However, on closer visual inspection (aided by the discriminant analysis; see § 4), it turns out that a *decreasing* standard deviation preferentially occurs prior to the flares. This may simply represent small-number statistics; it may also reflect a simplification of the lowest energy field configuration for the boundary condition. The only way for the potential field configuration to become simpler, in the context of the MCC model, is by way of reconnection, which cannot take place until a large enough current has built up along a separator loop.

Moments of the distribution of the distance between connected source pairs are also calculated, specifically, the distance between connected sources weighted by the magnetic flux in that connection (r_{ij}, ψ); two moments are shown in Figure 7. A simple bipolar region may have a fairly homogeneous distribution of connection lengths, while a more complex region may be expected to display both shorter and longer connections. *Changes* in the distance may be particularly important, as they would result in currents along separators. We see for these three fairly large active regions a very similar weighted mean connection length $\overline{(r_{ij}, \psi)}$, in contrast to a distinct difference between the flaring active regions and flare-quiet AR 8891 in the standard deviation $\sigma(r_{ij}, \psi)$; this difference is reflected in this parameter's appearance in a well-performing four-variable discriminant function (see § 4). This is another example of the remarkable constancy of some of the mean values of the MCT parameters between different active regions and also provides a clear indication of the *evolution* of some of the parameters. In many cases, trends in the parameters cannot be clearly distinguished from noise, but the mean distance for AR 8636 is clearly increasing. While such a trend might be expected to result in a flare, it continues to be present immediately after the flare in AR 8636, while no such trend is evident prior to either of the flares in AR 10030.

For connected source pairs, we define the tilt angle as the angle between the north/south axis and a line connecting from the positive source to the negative source:

$$\xi_{ij} = \tan^{-1}\frac{x_j - x_i}{y_j - y_i}. \tag{8}$$

We consider the moments of the distribution of ξ_{ij} weighted by the flux in the connection, so that connections to small sources in the plage do not make a large contribution, and we take the absolute value of the odd moments of the distribution to avoid hemispheric influences. For a simple bipolar region, the tilt angle should basically agree with Joy's law of active region tilt angles. More complex active regions will have a distribution of tilt

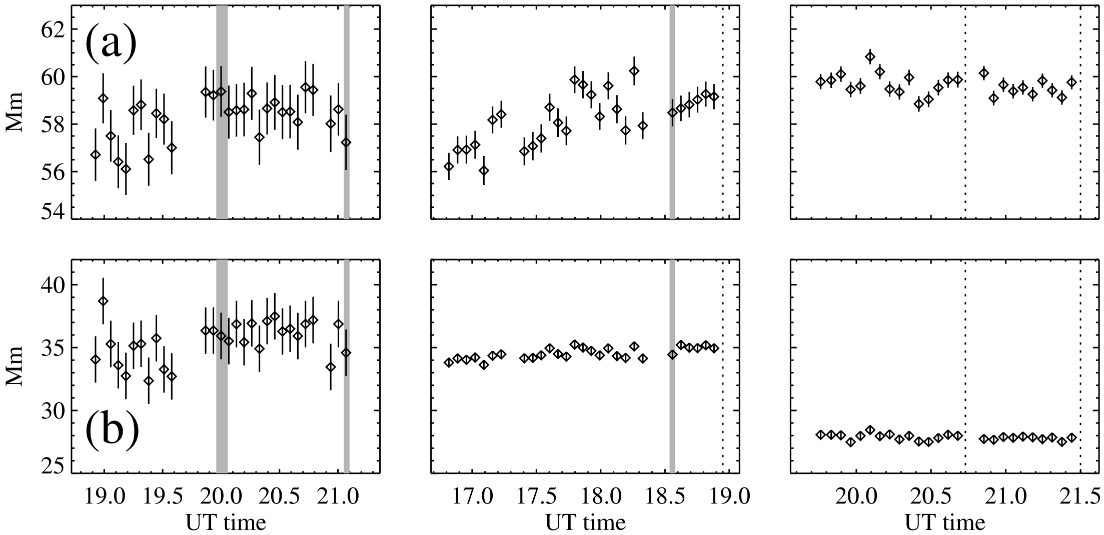

FIG. 7.—Same as Fig. 3, but for the first two moments of the distance between sources weighted by the domain flux, (*a*) $\overline{(r_{ij}, \psi)}$ and (*b*) $\sigma(r_{ij}, \psi)$.

angles, and emergence of new flux can result in the formation of new connections inconsistent with the mean, such as in the emergence of a polarity-reversed "δ-spot." Such an event should manifest as a change in the moments of the tilt-angle distribution, some examples of which are shown in Figure 8. In this case there is in fact an obvious difference between the flare-producing and flare-quiet active region(s) for the highlighted epochs.

3.3. *Magnetic Null Points*

The locations where the photospheric field is zero as prescribed by the MCT model, namely, the magnetic null points, are directly related to the coronal topology of the active region, as the fan surfaces of the null points compose the separatrices. It may be the case that simply characterizing the locations and distribution of the magnetic null points sufficiently describes a region's topology. Significant computational time could, in this way, be saved by negating the need to actually locate the magnetic separator field lines.

We consider the total number of both upright nulls, whose spines lie in the photospheric plane, and prone nulls, whose fan surfaces lie in the photospheric plane. Opposite to what might be expected, Figure 9 shows that the number of nulls and the number of upright nulls appear to be larger overall for the flare-quiet AR 8891 than the other two active regions highlighted here. While there appears to be an increase in the number of prone nulls after the two M class events (the sudden character due to the beginning of a new epoch), any such increase after the X class flare (also the beginning of a new epoch) is barely significant. Thus, the conclusion from examining this small number of regions and events is contrary to what we might expect concerning flare-predicting parameters.

3.4. *Magnetic Separators*

Reconnection during flares appears to occur along separators (Mandrini et al. 1991; Démoulin et al. 1993; Longcope & Silva 1998). The number of separators thus indicates the number of possible locations for a flare to occur. Magnetic complexity can be related not only to the number of separators present, but their spatial distribution as well.

Local concentrations of magnetic separators may allow not just a single energetic event, but also homologous or cascading events. In the context of the MCC model, this was interpreted as

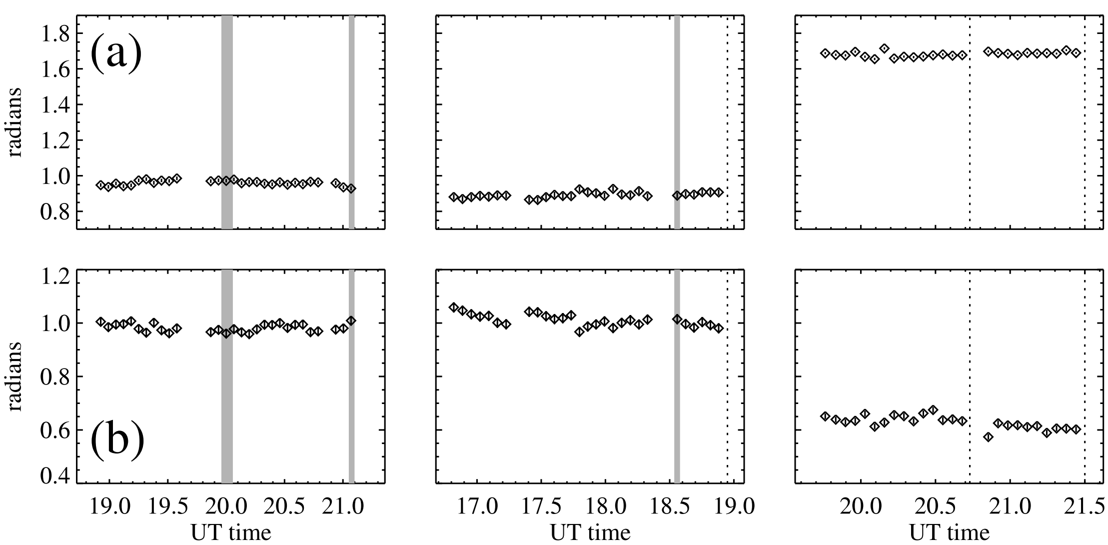

FIG. 8.—Same as Fig. 3, but for the first two moments of the tilt angle (weighted by the domain flux) of connected source pairs (*a*) $\overline{(\xi_{ij}, \psi)}$ and (*b*) $\sigma(\xi_{ij}, \psi)$ (see text and Table 3).

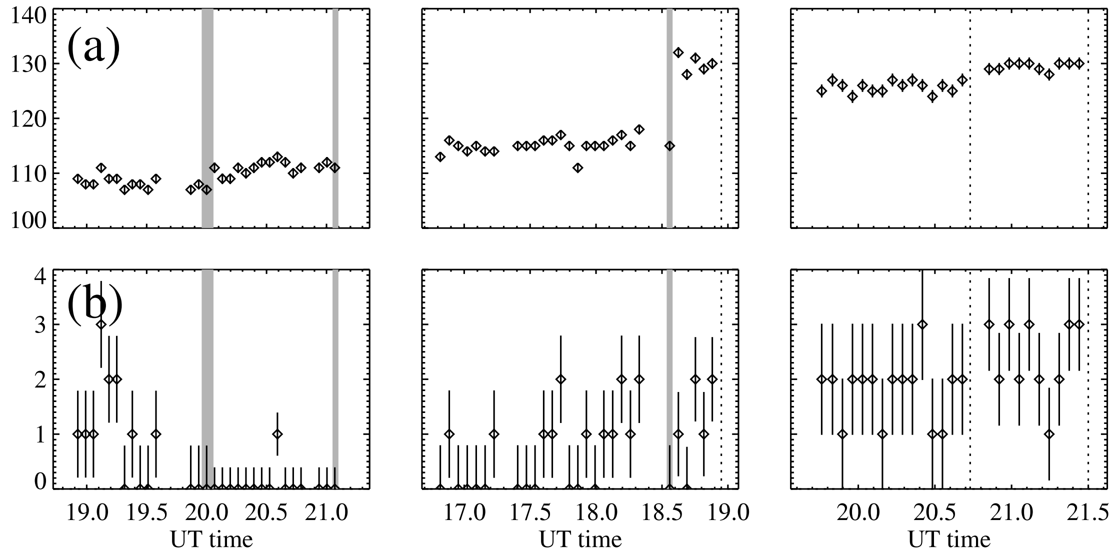

FIG. 9.—Same as Fig. 3, but for the total number of (*a*) prone, N_{p0}, and (*b*) upright, N_{u0}, magnetic nulls.

the result of the mutual inductance between neighboring separator loops giving rise to sympathetic flaring (Longcope & Silva 1998). In addition, the presence of multiple separators on a single null point has implications for the flow of currents along the separators. In the absence of reconnection, a domain flux remains constant by inducing a current to flow along the separator circuit that encloses it (Longcope & Klapper 2002). Multiple separators on a single null lead to more complicated separator circuits, including cases in which one separator is a member of more than one separator circuit. Thus, we consider a variety of parameters derived from the distribution of separators inferred from the MCT analysis of time series data.

The total number of separators is shown in Figure 10; AR 8636 has a slightly greater total number of separators than the other two regions, even more than AR 10030 prior to its X class event, although given the range of number of separators possible, these three active regions are remarkably similar. The trends in the number of separators with time appears also to be opposite between AR 10030 and AR 8636, the former's decreasing trend mirroring the trend in the flare-quiet AR 8891 during these observations.

We characterize the distribution of separators by the moments of the distribution of the number of separators associated with each null. The evolution of $\sigma(X_i)$ is shown in Figure 10 and again, the consistency with time and between active regions is striking. This is not surprising, given the relationship between the number of separators and the number of domains, and the consistency in the number of connections found (see Fig. 10), but it is a nice confirmation, since the connections and separators are located independently.

The distribution of separator lengths is calculated to determine whether shorter or longer separators are more indicative of flaring activity (Fig. 11). In addition, we examine the distribution of separator heights, which might provide clues as to whether reconnection preferentially occurs in the chromosphere or corona. From the three regions highlighted here, it appears the flaring regions favor shorter separator lengths with a more skewed distribution. The results for the height distribution for these three

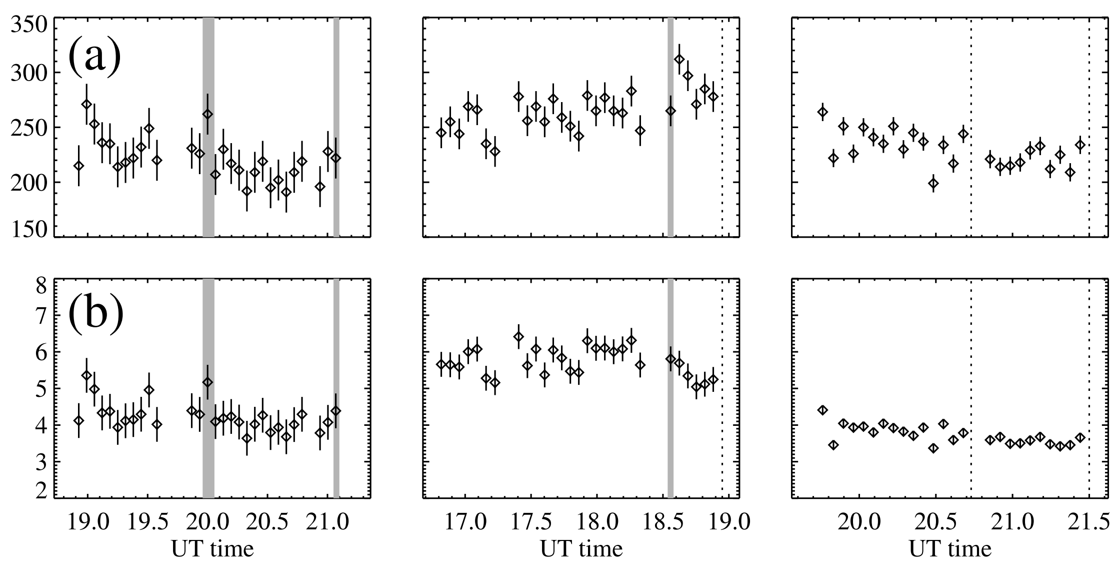

FIG. 10.—Same as Fig. 3, but for (*a*) the total number of separators *X* and (*b*) the standard deviation of the distribution of the number of separators associated with each magnetic null point, $\sigma(X_i)$.

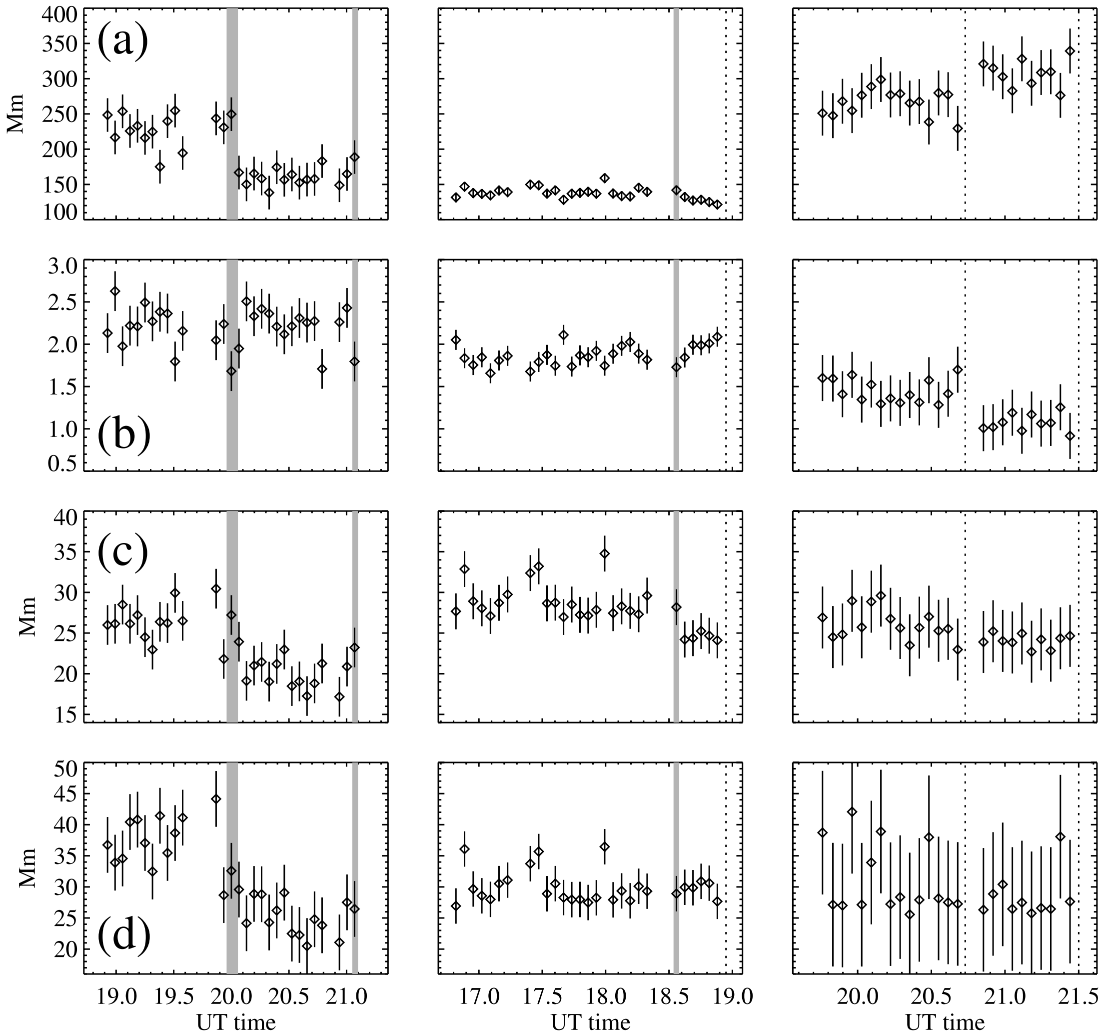

FIG. 11.—Same as Fig. 3, but for moments of the distribution of separator lengths (*a*) $\overline{l_i}$ and (*b*) $\varsigma(l_i)$ and for moments of the distribution of separator heights (*c*) $\overline{z_i}$ and (*d*) $\sigma(z_i)$.

regions is inconclusive from this visual test, although it is of interest that the separators for all three regions have an average height of approximately 25 Mm (well into the corona), with significant standard deviations, indicating the existence of both tall and short separator field lines. Further discussion follows in § 4.

A region is complex not only due to the number of separators but also their spatial distribution. As shown in BLL, multiple domains can link the same pair of sources. Because deducing the presence of multiple domains directly from tracing field lines is impractical, we rely on the hypothesis that the presence of more than one domain between two sources will always result in a pair of separators forming a loop between the same two null points. By enumerating the separators connecting the same pair of nulls, we infer the number of multiple domains. It turns out such configurations are not rare in the corona, and occasionally we find not just a looped pair of separators, but three or even four separators between the same two null points. We define the number of "excess domains," D_m, to be the total number of domains minus the number of connections. We infer the value of D_m by assuming that each separator in excess of one between a given pair of nulls corresponds to one excess domain. Since we do find pairs of nulls connected by three or more separators, we consider not just the number of excess domains, D_m, as inferred by the number of looped separators, but also L, the number of pairs of nulls that are connected by *at least* two separators. Such multiple domains may be of particular interest, because the looped pairs of separators result from one separatrix surface partially passing through a second separatrix surface, which indicates that reconnection must have happened at some prior stage. The evolution of D_m, the number of excess domains, is shown in Figure 12.

As a region evolves, the possibility of reconnection is intimately linked with the magnitude of the current that can flow along the separator field line, according to theories of reconnection along separators (Longcope 1996). A large amount of magnetic flux enclosed by a separator field line could, in principle, induce a larger current along the separator more readily than a small flux system. We compute the flux enclosed by a separator from the integral of the vector potential along a closed loop consisting of the separator and its image in the mirror corona,

$$\Psi_i = \frac{1}{2} \oint_{\mathcal{L}_i} \boldsymbol{A} \cdot d\boldsymbol{l}. \tag{9}$$

These fluxes can be related to the domain fluxes by way of a loop vector, $\Psi_i = \boldsymbol{Q}_i \cdot \boldsymbol{\psi}$ (Longcope & Klapper 2002). This quantity is signed by definition, and to avoid hemispheric or dominant-spot polarity bias, we consider the total of the unsigned flux and the moments of its distribution (Table 3). Examples are shown in

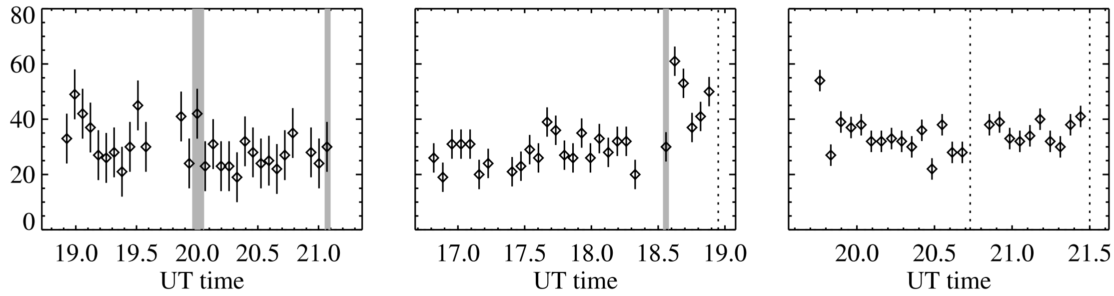

FIG. 12.—Same as Fig. 3, but for the number of "extra" domains, D_m.

Figure 13. In this case, the total flux enclosed does not provide a unique flare-productive result, although the higher order moments do indicate a difference between the two flare-producing active regions and the flare-quiet AR 8891. Further statistical analysis is described in § 4.

4. DISCRIMINANT ANALYSIS ON MCT PARAMETERS

Can the magnetic topology of the corona, as described using parameterizations derived from the MCT model applied to photospheric vector field data, distinguish between flare-imminent and flare-quiet epochs during an active region's evolution? Consideration of individual parameters for a few selected regions is ambiguous, so to examine this question we turn to a statistical approach that simultaneously considers multiple variables: discriminant analysis (e.g., Kendall et al. 1983; Anderson 1984). Parameter space is divided into two regions, such that measurements from a new epoch that fall in one of the regions are predicted to flare, while measurements that fall in the other region are predicted to be flare-quiet. The discriminant function is the boundary between the two regions, constructed so as to maximize the overall rate of correct predictions. Under the assumptions described in Paper II, including that the population distributions are Gaussian with equal covariance matrices, the discriminant function is a hyperplane, which is simply a line in two dimensions.

In addition to discriminant analysis (DA), we use a T^2-test to determine the probability that the flaring and flare-quiet samples come from different populations. The T^2-test essentially measures the distance between the means of the two samples in appropriately standardized units; it does not, however, indicate how much overlap between the populations there is, as DA does. Thus, we employ the combination of the two analyses.

The mechanics of this statistical analysis follow Paper II exactly, including the active regions considered and the epochs defined; for clarity we summarize the relevant data here (see Table 1). In this case, we have samples from epochs that ended in a flare and samples from epochs that were flare-quiet. The mean of each variable for each epoch is considered, to quantify flare-relevant thresholds. In addition, a linear regression line is fit to each variable for each epoch, and the slope of the line is used to quantify the variable's evolution over the epoch. We denote the mean value of a variable for an epoch by $\langle x \rangle$, and the slope of the variable by dx/dt. We have defined 51 parameters, consisting of 11 single measures, plus the four moments of an additional 10 measures. For each parameter, we consider both the mean and the slope, resulting in a total of 102 different variables. Below, we present a two-variable discriminant function as an initial example. The best- and worst-performing variables are discussed next, as evaluated individually; finally, we showcase some two- and four-variable combinations with relevant

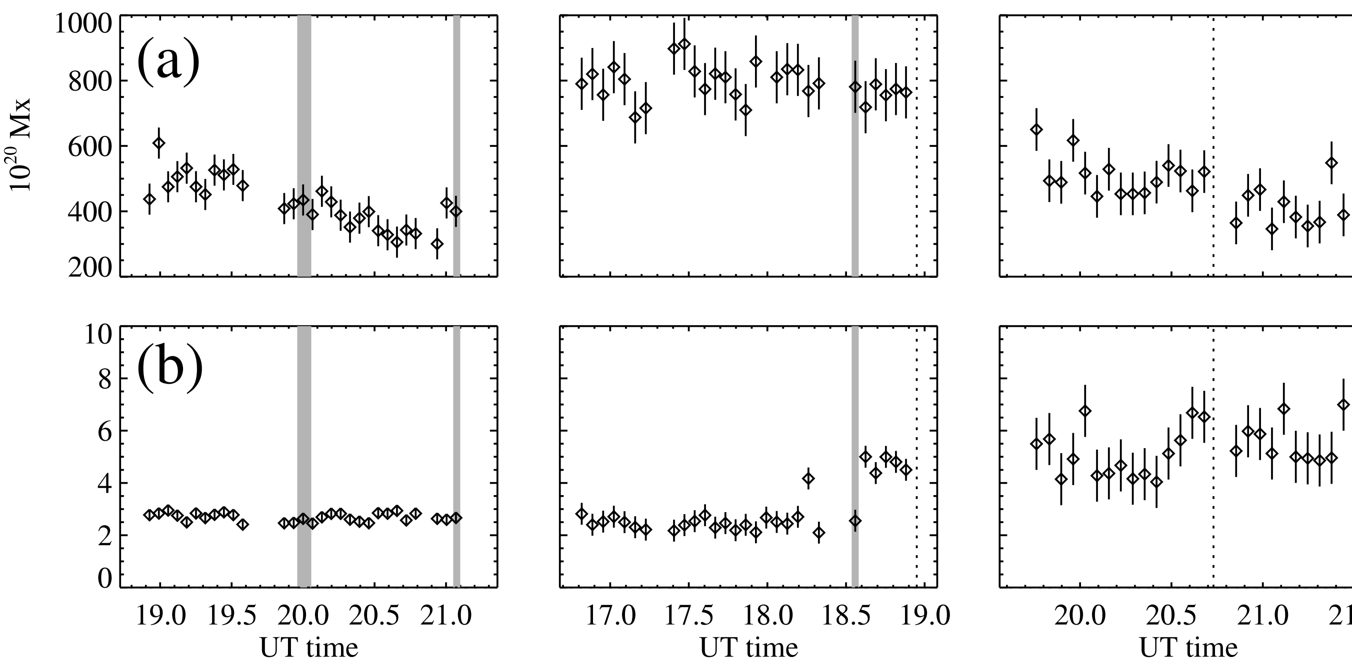

FIG. 13.—Same as Fig. 3, but for (*a*) the total flux enclosed by the separators $|\Psi|_{\rm tot}$ and (*b*) the skew of the distribution of fluxes enclosed by separators $\varsigma|\Psi_i|$.

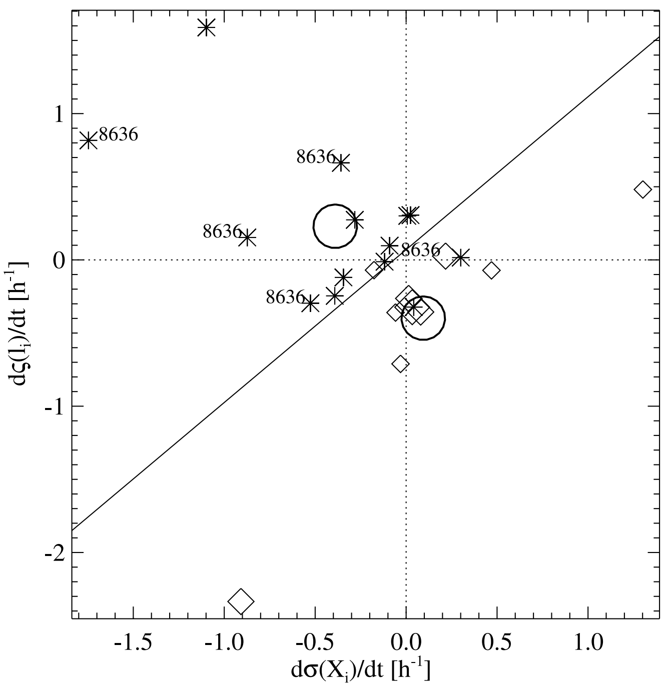

FIG. 14.—Discriminant function for the variables $d\sigma(X_i)/dt$, $d\varsigma(l_i)/dt$. Diamonds indicate flaring epochs and are sized by the flare class, with the smallest being C class, intermediate being M class, and the largest being X class; asterisks indicate quiet epochs. The discriminant function is shown by the solid line, and the mean of each sample is indicated by a large circle. A new epoch that falls below and to the right of the line would be forecast to flare, while one above and to the left of the line would be forecast to be flare-quiet. One active region (AR 8636) has been labeled to give an indication of the amount of scatter between epochs.

comparisons to the photospheric vector field data results from Paper II.

4.1. *A Two-Variable Example*

As a demonstration of DA, we show in Figure 14 a plot of two variables derived from the MCT analysis that performed unexpectedly well: the slope of the standard deviation of the distribution of the number of separators on each null versus the slope of the skew of the distribution of separator lengths (see Figs. 10 and 11). The mean of the flaring population has an increasing $d\sigma(X_i)/dt$ but a decreasing $d\varsigma(l_i)/dt$, implying that in the flaring regions the lengths of separators were becoming more homogeneous, although the distribution of them among nulls was in fact becoming less so. This pair correctly classifies 87.5% of the points (Table 4), which is significantly better than any two-variable pair using the photospheric parameters in Paper II. It also returns a probability that the samples indeed represent two different populations of 0.974, compared to 0.943 from the best photospheric two-variable combination. We caution that this is a demonstration only, with far fewer data points than adequate for a robust interpretation.

TABLE 4

CLASSIFICATION TABLE FOR $d\sigma(X_i)/dt$ AND $d\varsigma(l)/dt$

	PREDICTED	
OBSERVED	Flare	No Flare
Flare	9	1
No flare	2	12

TABLE 5

10 BEST PERFORMING SINGLE-VARIABLE DA RESULTS

Variable	Probability	Error Rate
dD_m/dt	0.895	0.292
$d\varsigma(l_i)/dt$	0.886	0.333
dL/dt	0.885	0.333
$d\sigma(X_i)/dt$	0.840	0.333
$d\sigma(z_i)/dt$	0.817	0.417
$d\kappa(l_i)/dt$	0.811	0.375
$\langle\kappa(\Psi_{ij})\rangle$	0.801	0.375
$\langle\varsigma(\Psi_{ij})\rangle$	0.781	0.375
dX/dt	0.780	0.292
$d\kappa(\xi_{ij}, \psi)/dt$	0.720	0.458

4.2. *Results for Single- and Multiple-Variable DA Combinations*

It quickly becomes apparent that any single quantity will rarely, if ever, provide a unique flare-imminence predictor. This was demonstrated in Paper II for variables directly characterizing the photospheric vector field maps and is fairly evident from the examples and discussion in § 3. How well did any of our variables do with the full 24-epoch data set? By sorting based on the probabilities that the two samples are indeed different populations, i.e., following the procedure in Paper II, we find that the best single parameter, dD_m/dt, achieves an 0.895 probability that the data sample different populations (Fig. 12; Table 5). This is significantly higher than the 0.703 found using single variables characterizing the photospheric field as derived in Paper II. Although the resulting classification table is only about 71% correct, the means of this parameter for the two populations imply a physical interpretation that flare events are preceded by a slight increase in the number of domains in excess of the number of connections, whereas during flare-quiet epochs this quantity is decreasing.

Recalling that the probability is based on the characterization of the two sample sets that reveals different information than the classification table, we also highlight the single variable $d\sigma(\varphi_{ij})/dt$, which returns a probability of 0.510, but also returns the highest scoring classification table, with 75% correct (Table 6). For this variable, the unbiased estimate of the error rate given by the $n-1$ approach described in Paper II is 0.250, matching the classification table, but the sample means imply a preflare *decrease* in $d\sigma(\varphi_{ij})/dt$ and increases during quiet epochs.

The real power of discriminant analysis, of course, is the ease with which multiple parameters can be combined, sometimes with dramatic improvements. The two-variable combination resulting in the highest probability of 0.986 is the combination $d\kappa(r_{ij},\psi)/dt$, $d\varsigma(l_i)/dt$. There are five additional combinations with probabilities of sampling different populations above 0.970. These combinations result in classification tables that score between 75% and 87.5% correct. The combination $d\sigma(\Phi_i)/dt$, dD_m/dt results in the best classification table, at 91.7% correct (two misclassifications), although it has a probability of 0.965 of sampling different populations.

TABLE 6

CLASSIFICATION TABLE FOR $d\sigma(\varphi_{ij})/dt$

	PREDICTED	
OBSERVED	Flare	No Flare
Flare	7	3
No flare	3	11

TABLE 7

Classification Table for $d\varsigma(\psi_{ij})/dt$, $d\sigma(X_i)/dt$, $d\varsigma(l_i)/dt$, $d\langle\sigma(r_{ij})\rangle/dt$

	Predicted	
Observed	Flare	No Flare
Flare	10	0
No flare	0	14

Extending the multiple-variable analysis, we find that for four-variable DA, the best probability-scoring combinations all have probabilities above 0.999. The top-scoring four-variable function is

$$f = 0.608 - 12.37\frac{d}{dt}C + 10.8685\frac{d}{dt}\sigma(C_i) - 4.82\frac{d}{dt}\kappa(\psi_{ij}) + 7.90\frac{d}{dt}L, \tag{10}$$

with a T^2 probability of 0.9999 and a classification table success of 87.5 (three misclassifications). The magnitude of the coefficients indicates the relative "predictive power" of the four variables within this function, so dC/dt, the rate of change of the total number of connections, is the variable with the most predictive power. As an interesting contrast, consider the four-variable function

$$f = 0.26 - 1.02\frac{d}{dt}\varsigma(\psi_{ij}) + 1.80\frac{d}{dt}\sigma(X_i) - 1.62\frac{d}{dt}\varsigma(l_i) + 1.09\langle\sigma(r_{ij}, \psi)\rangle, \tag{11}$$

which has a probability of sampling different populations of 0.994, but produces a perfect classification table (Table 7).

Two points are of special interest. First, we reiterate that the key to producing a high-probability or successful classification table is not necessarily the variables themselves, but the appropriate *combination* of variables (see discussion in Paper II). The discriminant function created with the four best single-variable–scoring parameters (Table 5) returns a probability of distinct populations of 0.9758 and 87.5% correct classification: not particularly terrible, but by no means the best four-variable combination.

Second, what is especially interesting is that similarly high probability scores and successful classification tables were *only* possible for the photospheric magnetic field properties in Paper II with combinations of six variables. The best four-variable combinations derived for the photospheric data result in a probability of 0.9996 and a one-miss classification table. This is despite considering more variables characterizing the photospheric field than the coronal field (160 vs. 102). A pessimistic interpretation invokes problems arising from small-number statistics, a realm in which these data certainly exist. The optimistic interpretation of this result is that by inferring the topology of the corona, more appropriate information concerning impending reconnection is gleaned than when only considering the magnetic structure at the photospheric boundary.

5. DISCUSSION

We demonstrate here the application of MCT analysis to time series of active region vector magnetic field maps, in the context of determining what causes a flare. Earlier studies focused on physical quantities describing the photospheric vector magnetic field, such as the distribution of the field morphology, vertical current densities, inferred force-free twist parameters, etc. (see discussion and references in Paper I). The focus for predictive tests such as the present one is on the state and variation of relevant quantities immediately prior to flare events, with control data points of epochs ending in no flare event. It was shown in Paper II that the analysis of photospheric vector magnetic field data could, with an adequate number of variables considered simultaneously, successfully distinguish between flare-imminent and flare-quiet samples. The focus was, however, primarily the demonstration of a statistically rigorous method of addressing the question of what role photospheric fields and their evolution may play in producing a solar flare.

In the present study we bring the focus up into the corona, where it is assumed that the magnetic reconnection necessary for solar flares occurs. With the hypothesis that magnetic reconnection can occur in the vicinity of magnetic separators, we present here a method to test the hypothesis statistically. We parameterize the character of active region coronae as modeled with MCT, including not only the distribution of magnetic separators, but other descriptors of the coronal magnetic complexity, such as the connectivity matrix, domain fluxes, and magnetic null points.

Despite sometimes wide ranges in the global MCT properties of the active regions, including quantities such as the total number of sources needed to represent the region, we find that on average there is remarkable consistency between the targeted regions, particularly in quantities such as the mean number of connections between sources. However, there were clear indications that some regions contained large, local variations in the MCT properties, as evidenced by the differences for the higher order moments. There were also clear indications of evolution in some parameters for some of the regions. Since all of the regions we considered produced flares at some point in their lifetimes, it appears that what determines a flare may be tied into local properties and changes of the regions.

Using the same samples as Paper II, but with fewer total variables, we find that the best coronal descriptors lead to higher probabilities of distinguishing the two populations than we achieved using quantities solely characterizing the photosphere. Single-variable discriminant functions from the MCT parameters performed better than single-variable quantities from photospheric parameters, as did two- and four-variable discriminant functions. This result held, regardless of the evaluation criterion used, either the probability of distinguishing the two populations or the classification rate for the resulting discriminant function. A striking example is the ability to generate a 100% correct classification by simultaneously considering four variables for the MCT parameters, whereas a similar feat required six variables for photospheric parameters for the given data set.

Does this imply that the answer to what produces a solar flare lies in the temporal variation of the skew of the distribution of the flux in the connections? No. While we approach this question statistically with suitable control data, we are still in the realm of small-number statistics. Although the importance of any specific parameter is dubious at best, the fact that the overwhelming majority of our best parameters are slopes may not be, for two reasons. First, the regions we consider were all expected to flare and all did so, although not necessarily during our observation periods. Thus, we expect that all the regions contain sites for reconnection to occur, with sufficient energy to power a flare. What is lacking for the flare-quiet epochs under consideration is a trigger. We propose that a trigger will be seen as a *change* in some property of the active region, so the frequent appearance of slopes in the best parameters may be expected. A second, not necessarily mutually exclusive reason is that the temporal variations produce more randomly distributed variables, whereas the parameters' means tend to cluster together by active region, and the former may lead more easily to spurious results, indicating differences between flaring and flare-quiet epochs.

At this juncture, we optimistically put forward that there is more information contained in the morphology and topology of the coronal field relevant to producing a flare-ready solar atmosphere than is available by characterizing the photospheric field. We also acknowledge that this may still be an artifact of small-number statistics and declare that no definite conclusion can be drawn without much more data. The regions in this study were chosen in part because each flared at some point, even though it was not necessarily during the period of observation considered here. Despite the large archive of IVM data, the number of time series of such regions is relatively small, providing at most a few hundred epochs. It may rather be that we must wait for upcoming space-based vector magnetographs to accumulate a sample large enough to make our results statistically significant.

Even though the MCT model has at its heart the simplest field extrapolation method, this model is probably better able to quantify those pieces of information that can distinguish between the two populations in question here. Thus, we postulate that while again there is no obvious single parameter that can uniquely characterize a flare-imminent corona, combinations of parameters that characterize the coronal magnetic topology are more appropriate for this question than the results of staying down in the photosphere.

The authors would like to thank F. A. F. for useful contributions to this manuscript, Dana Longcope for his insights into MCT, and the second referee for taking the time to understand the present results in the context of previous work. This work was carried out at the Colorado Research Associates Division of NorthWest Research Associates with data from the University of Hawaii Mees Solar Observatory. Funding from the Air Force Office of Scientific Research under contracts F49620-00-C-0004 and F49620-03-C-0019 is gratefully acknowledged.

REFERENCES

Abramenko, V. I., Yurchyshyn, V. B., Wang, H., Spirock, T. J., & Goode, P. R. 2003, ApJ, 597, 1135
Anderson, T. W. 1984, An Introduction to Multivariate Statistical Analysis (New York: Wiley)
Aulanier, G., DeLuca, E. E., Antiochos, S. K., McMullen, R. A., & Golub, L. 2000, ApJ, 540, 1126
Barnes, G., Longcope, D. W., & Leka, K. D. 2005, ApJ, 629, 561 (BLL)
Baum, P. J., & Bratenahl, A. 1980, Sol. Phys., 67, 245
Canfield, R. C., et al. 1993, ApJ, 411, 362
Démoulin, P., Henoux, J. C., & Mandrini, C. H. 1994, A&A, 285, 1023
Démoulin, P., van Driel-Gesztelyi, L., Schmieder, B., Hénoux, J. C., Csepura, G., & Hagyard, M. J. 1993, A&A, 271, 292
Falconer, D. A., Moore, R. L., & Gary, G. A. 2003, J. Geophys. Res., 108, 11
Gorbachev, V. S., & Somov, B. V. 1988, Sol. Phys., 117, 77
Jing, J., Yurchyshyn, V. B., Yang, G., Xu, Y., & Wang, H. 2004, ApJ, 614, 1054
Kendall, M., Stuart, A., & Ord, J. K. 1983, The Advanced Theory of Statistics, Vol. 3 (4th ed.; New York: Macmillan)
Kundu, M. R., Nindos, A., & Grechnev, V. V. 2004, A&A, 420, 351
LaBonte, B., Mickey, D. L., & Leka, K. D. 1999, Sol. Phys., 189, 1
Lau, Y.-T. 1993, Sol. Phys., 148, 301
Leka, K. D., & Barnes, G. 2003a, ApJ, 595, 1277 (Paper I)
———. 2003b, ApJ, 595, 1296 (Paper II)
Liu, Y., & Kurokawa, H. 2004, ApJ, 610, 1136
Longcope, D. W. 1996, Sol. Phys., 169, 91
Longcope, D. W., & Klapper, I. 2002, ApJ, 579, 468
Longcope, D. W., & Magara, T. 2004, ApJ, 608, 1106
Longcope, D. W., & Silva, A. V. R. 1998, Sol. Phys., 179, 349
Mandrini, C. H., Démoulin, P., Hénoux, J. C., & Machado, M. E. 1991, A&A, 250, 541
Mickey, D. L., Canfield, R., LaBonte, B. J., Leka, K. D., Waterson, M. F., & Weber, H. M. 1996, Sol. Phys., 168, 229
Parnell, C. E., Priest, E. R., & Golub, L. 1994, Sol. Phys., 151, 57
Priest, E. R., & Démoulin, P. J. 1995, Geophys. Res., 100, 23443
Priest, E. R., & Forbes, T. G. 1989, Sol. Phys., 119, 211
Uddin, W., Jain, R., Yoshimura, K., Chandra, R., Sakao, T., Kosugi, T., Joshi, A., & Despande, M. R. 2004, Sol. Phys., 225, 325
Van Ballegooijen, A. A., & Martens, P. C. H. 1989, ApJ, 343, 971
Wang, H. 2005, ApJ, 618, 1012